



POLITECNICO
MILANO 1863

**SCUOLA DI INGEGNERIA INDUSTRIALE
E DELL'INFORMAZIONE**

Interplanetary Explorer Mission - Planetary Explorer Mission

ORBITAL MECHANICS

Group ID: 2406

Student ID	Surname	Name
10806725	Richero	Giovanni
11060088	Emrem	Mert
10773250	Bernasconi	Ludovico
10796973	Serlini	Mariagiulia

Professor: Prof. Camilla Colombo
Academic Year: 2024-25

Contents

1 Assignment I:	
Interplanetary Explorer Mission	
1.1 Structure of Analysis	1
1.2 Preliminary Analysis	2
1.3 Grid Search	2
1.3.1 Cost Grid Construction for Lambert arcs	2
1.4 Optimization Methodologies	4
1.5 Outcome and Results	5
1.6 Overall Mission Trajectory	5
1.6.1 Mars Fly-by	6
2 Assignment II:	
Planetary Explorer Mission	
2.1 Orbit Characterization	7
2.2 Ground Track	8
2.3 Repeating Ground Track	8
2.4 Perturbed Orbit Propagation	10
2.4.1 Results Filtering	10
2.5 Real World Data Analysis	12
References	13

1 | Assignment I: Interplanetary Explorer Mission

This assignment involves the design of a mission that begins from Mercury (☿), executes a flyby at Mars (♂) and concludes in Asteroid No. 40 (henceforth referred to as Harmonia or A40). The mission is required to begin no earlier than the January 1, 2030 and conclude no later than December 31, 2059. The spacecraft is assumed to depart and arrive with velocities matching those of the departure and arrival bodies, eliminating the need to account for orbit insertion or deorbit maneuvers and their associated ΔV requirements.

1.1. Structure of Analysis

The feasibility of a mission is primarily driven by the required ΔV and the mission duration. This holds true for the current mission, which is expected to be demanding in terms of ΔV , given the selected destinations.

The mission trajectory consists of three conic sections connected sequentially, modeled using the patched-conics method. Two of these sections are solutions to *Lambert's Problem*, which provides the unique ΔV requirements for a given set of parameters: initial position (\vec{r}_i) and time (t_i), final position (\vec{r}_f) and time (t_f), and time of flight (ToF = $t_f - t_i$). In our case,

- for the first leg : $\vec{r}_i = \vec{r}_{\text{☿}}$, $\vec{r}_f = \vec{r}_{\text{♂}}$, ToF₁ $\Rightarrow \Delta V_{i,1}, \Delta V_{f,1}$
- for the second leg : $\vec{r}_i = \vec{r}_{\text{♂}}$, $\vec{r}_f = \vec{r}_{\text{A40}}$, ToF₂ $\Rightarrow \Delta V_{i,2}, \Delta V_{f,2}$

The remaining segment is the flyby hyperbolic trajectory at Mars. Here, the hyperbolic trajectory connects the inbound and outbound velocity vectors, defined as $\vec{v}_{\infty-}$ and $\vec{v}_{\infty+}$, derived from the velocity changes at the end of the first leg ($\Delta V_{f,1} = \vec{v}_-$) and the start of the second leg ($\Delta V_{i,2} = \vec{v}_+$). The velocity relationships are expressed as:

$$\vec{v}_{\infty-} = \vec{v}_- - \vec{v}_{\text{♂}}; \quad \vec{v}_{\infty+} = \vec{v}_+ - \vec{v}_{\text{♂}} \quad (1.1)$$

The hyperbolic trajectory connecting the inbound and outbound velocities may end up not being realizable, as determined by the maximum turn angle δ of the flyby. In such a case, an impulse is required during the flyby to *match* the two velocities, making the flyby a powered gravity assist (PGA). The ΔV of the impulse at the pericenter of the flyby is defined as the difference of velocity at pericenter of the inbound leg of the hyperbola (v_{p-}) and the one of the outbound leg (v_{p+}).

$$\Delta V_{\text{PGA}} = |v_{p+} - v_{p-}| = \left| \sqrt{v_{\infty+}^2 + \frac{2\mu_{\text{♂}}}{r_p}} - \sqrt{v_{\infty-}^2 + \frac{2\mu_{\text{♂}}}{r_p}} \right| \quad (1.2)$$

The analysis aims to find the best combination between these three arcs that minimizes that total cost:

$$\Delta V_{\text{total}} = \Delta V_1 + \Delta V_2 + \Delta V_{\text{PGA}} \quad (1.3)$$

The variables that determine ΔV_{total} are dates of departure (t_{dep}), flyby (t_{flyby}), and arrival (t_{arr}). Therefore, 3 degrees of freedom (DoFs) are available to optimize the transfers.

1.2. Preliminary Analysis

The problem is initially defined by ranges of permissible departure and arrival dates, which includes transfers that are infeasible either due to time or ΔV . To eliminate parts of this search space, the feasible arrival window range was preliminarily estimated through the synodic periods of the relevant bodies. Synodic period, T_{syn} is found as follows.

$$T_{\text{syn}} = \frac{T_1 \cdot T_2}{|T_1 - T_2|} \quad (1.4)$$

where subscripts 1 and 2 denote the two bodies, in our case, Mercury-Mars and Mars-Harmonia. The longer of the two synodic periods is the one between Mars and Harmonia ($T_{\text{syn},2}$) at about 4.2 years. However, due to Harmonia's orbital inclination and eccentricity, its position relative to Mars shifts after each synodic period and cycles at the least common multiple of synodic period and the slower orbit [1], therefore, a more conservative window was used considering $T_{\text{A40}} = 3.42$ years: $T_{\text{A40}} \cdot T_{\text{syn},2} \approx 14.33$ years.

As an initial approximation, the transfer costs and flight times are computed assuming that the planetary orbits are planar and circular. The ratios of the semi-major axes for the Mercury-Mars and Mars-Harmonia orbits are:

$$\frac{r_{\sigma}}{r_{\chi}} = 3.9365; \quad \frac{r_{\text{A40}}}{r_{\sigma}} = 1.4881; \quad (1.5)$$

This indicates that a Hohmann¹ transfer is the most efficient two-impulse maneuver for both legs [2], resulting in a $\Delta V_{\text{Hohmann, total}} = 25.66$ km/s. Although this estimate does not account for orbital eccentricity or inclination, it provides a reasonable baseline for our final results.

1.3. Grid Search

1.3.1. Cost Grid Construction for Lambert arcs

To compute the optimal total cost of the interplanetary trajectory, all possible combinations of Lambert arcs must be considered. The most straightforward approach involves constructing a 3D matrix that maps the mission cost across the three degrees of freedom (*DoFs*) by iterating through all combinations of departure, flyby, and arrival dates using three nested *for* loops.

However, a significant reduction in computational effort can be achieved by decoupling the two Lambert's problems. Instead of solving $l \times m \times n$ cases—where l , m , and n represent the number of discretized points for t_{dep} , t_{flyby} , and t_{arr} , respectively—the problem is split into two independent calculations:

1. Compute $l \times m$ cases for the first leg (Mercury to Mars).
2. Compute $m \times n$ cases for the second leg (Mars to Harmonia).

This approach produces two 2D matrices:

- **M₁**, which contains $\Delta V_{i,1}$ for each combination of t_{dep} and t_{flyby} .
- **M₂**, which contains $\Delta V_{f,2}$ for each combination of t_{flyby} and t_{arr} .

From these data, porkchop plots of the two Lambert arcs are generated, as shown in Figure 1.1 and Figure 1.2.

¹The bi-elliptic transfer becomes more efficient than the Hohmann transfer only when the ratio between the final and initial orbital radii exceeds 11.94

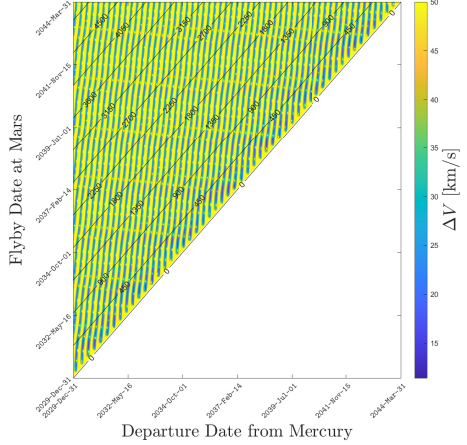


Figure 1.1: Porkchop plot - leg 1 ($\text{\textbf{\textit{♀}}}$ – $\text{\textbf{\textit{♂}}}$)

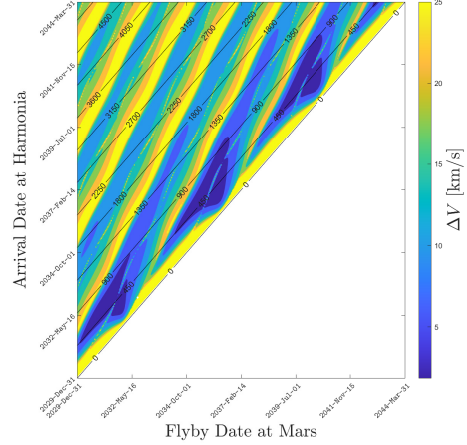


Figure 1.2: Porkchop plot - leg 2 ($\text{\textbf{\textit{♂}}}$ – $A40$)

In Figure 1.1 and Figure 1.2, we observe the repeating pattern characteristic of porkchop plots. These plots exhibit local minima that repeat every synodic period, with distinct features such as the central ridge down the middle of the ΔV valleys, which is attributed to the effects of orbital inclination. To take into account ΔV_{PGA} , we can extend each of these plots in a third dimension, and eliminating the dates where they do not intersect from analysis. Doing so eliminates negative ToF transfers. In our code, both \mathbf{M}_1 and \mathbf{M}_2 are given a maximum feasible ΔV value (e.g. $\Delta V_{\text{max}} = 20 \text{ km/s}$ per leg) to reduce the search space. The ΔV grid of the first leg, \mathbf{M}_1 , is repeated along the t_{arr} dimension, while the second leg, \mathbf{M}_2 , is repeated along t_{dep} . After rotation to align with the *DoFs* reference frame, \mathbf{M}_1 and \mathbf{M}_2 can be combined into a cloud of candidate points, with ΔV equaling their sum, as shown in Figure 1.3.

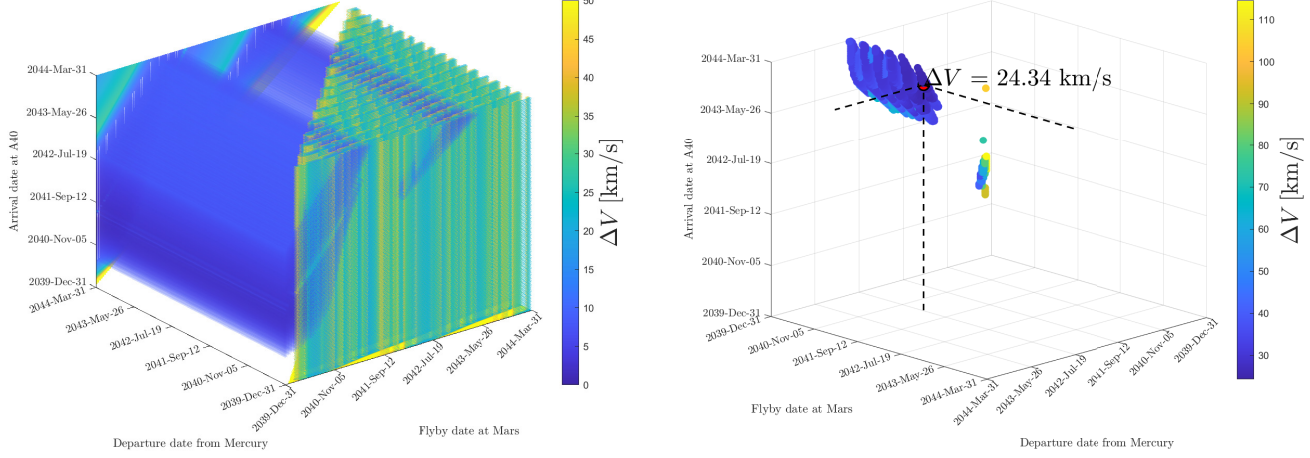


Figure 1.3: Left: Matrices \mathbf{M}_1 and \mathbf{M}_2 extended over time w.r.t. their respective third DoF. Right: The intersecting cloud of ΔV s with added conditions ($\Delta V_1 < 50$, $\Delta V_2 < 15[\text{km/s}]$)

As a result of the previous steps, the total gravity flyby calculations that needed to be done were reduced from $l \times m \times n$ cases to a drastically fewer count. In the case shown in Figure 1.3, candidate points were reduced from 3375000 to 74466 points by isolating intersections, then further reduced to 3021 points by applying a flyby radius constraint², after which, the ΔV_{total} is known at each point. More stringent limits yielded fewer candidate points. In Algorithm 1.1, the previously explained passages are reported.

²Further explained in section 1.4

Algorithm 1.1 Grid Search for Lambert's Problem

```
1: Inputs: departure_window, flyby_window, arrival_window, astro_constants
2: Outputs: List of valid trajectories
3: for each  $t_{\text{dep}}$  in departure_window do
4:   for each  $t_{\text{flyby}}$  in flyby_window do
5:     Compute leg 1: Solve Lambert's Problem  $\rightarrow \Delta V_1$ 
6:   end for
7: end for
8: for each  $t_{\text{flyby}}$  in flyby_window do
9:   for each  $t_{\text{arr}}$  in arrival_window do
10:    Compute leg 2: Solve Lambert's Problem  $\rightarrow \Delta V_2$ 
11:   end for
12: end for
13: Extract intersections from results of leg 1 and leg 2
14: for each trajectory  $i$  in intersections do
15:   if  $r_p(i) > R_{\text{Mars}} + h_{\text{atm}}$  then
16:     Compute  $\Delta V_{\text{PGA}}$  at  $i$ 
17:     Calculate  $\Delta V_{\text{total}}$  at  $i$ 
18:     Add  $i$  to valid trajectories
19:   end if
20: end for
21: Return: valid trajectories
```

1.4. Optimization Methodologies

To find an optimal value of ΔV_{total} , two different methodologies are used. First, constraints are applied to the solution. It was decided to limit the analysis to elliptical transfer arcs based on the Lambert's problem: this is reasoned by the fact that allowing the transfer orbit to be parabolic or hyperbolic would dramatically increase ΔV_{total} while reducing *ToFs*. Thus, the constraints are defined in terms of the eccentricities of the two Lambert arcs, denoted by e_1 and e_2 . These eccentricities are bounded by the following conditions: $0 \leq e_{1,2} < 1$, which ensures that the orbits are elliptical.

Additionally, a constraint is applied on the hyperbola connecting the two transfer legs, considering only the hyperbola satisfying $r_{P_\sigma} > R_\sigma + h_{\text{atm}}$ is the hyperbola's radius of pericenter³. This choice is based on physical feasibility⁴ of the transfer arc considering literature past flybys at Mars.

Hybrid Gradient-based Approach The first approach involve a constrained optimization method, combining the Grid Search Algorithm (1.1) with the MATLAB `fmincon` function. The function is a gradient-based optimizer that is capable of accurately finding a local minimum departing from a nearby initial guess and the convergence point will be highly dependent on this. For this reason, we decided to choose as a proper initial guess the local minimum obtained from the Grid Search Algorithm to force convergence.

Heuristic Approach The second approach performed the optimization using MATLAB `ga` function. In this case, the function is a genetic-based meta-heuristic optimizer called genetic algorithm. This last one works by:

1. Defining an initial population (first generation) formed by different combinations of allowed possibilities for the input optimization parameters (t_{dep} , t_{flyby} and t_{arr});

³where r_{P_σ} , R_σ is Mars' radius and h_{atm} is the max atmosphere altitude

⁴drag atmosphere would be negligible for $h > 200$ km; 220 km to be conservative

2. Evaluating a given fitness function Δv for each individual;
3. Choosing the better individuals, according to the fitness function, from the population and recombining their characteristics to form the next generation. In this passage some of the non-optimal individuals are added to improve diversity. This process is iterated until a point of sufficient value is found.

The optimization method `fmincon` requires an initial guess, and its success heavily depends on this starting point, but it is guaranteed to converge to at least a local minimum. In contrast, `ga` does not require an initial guess. However, as a heuristic approach rather than a rigorous mathematical method, it does not ensure finding the optimal solution.

The standalone and combined methods are executed both, using the time windows that are chosen in Section 1.2. After the first optimization run, we use the results to narrow the time windows and refine the grid for ΔV_{total} by adding more points across 3 *DoFs*, without exceeding the computational budget. By repeating this process, we identify the best reduced and refined time windows. Then, we test all combined approaches, starting with `ga` and refining it further with `fmincon`.

1.5. Outcome and Results

The following results are obtained:

Optimizer	Fitness function	ΔV_{total} [km/s]	Dates			n
			t_{dep}	t_{flyby}	t_{arr}	
Grid Search	[\cdot]	23.8720	29/3/2041 15:25:03	7/6/2042 16:42:04	3/8/2043 06:09:07	3
Hybrid: GS + fmincon	$\Delta v(t_{\text{dep}}, t_{\text{flyby}}, t_{\text{arr}})$	23.8377	29/3/2041 15:08:26	8/6/2042 08:43:59	5/8/2043 12:55:54	5
ga	$\Delta v(t_{\text{dep}}, t_{\text{flyby}}, t_{\text{arr}})$	23.8269	29/3/2041 11:27:14	7/6/2042 00:32:07	31/7/2043 22:44:57	20

Table 1.1: Optimization results. The number of trials is denoted by n .

As shown in Table 1.1, the Grid Search Algorithm 1.1 alone identifies an excellent alternative in terms of ΔV_{total} . However, the hybrid approach achieves convergence more quickly, as it does not require high-resolution grids as inputs. Given that `ga` consistently identifies the best overall solution, it is reasonable to assume that this solution could represent a global minimum.

1.6. Overall Mission Trajectory

The most optimal transfer in terms of cost among all available options is shown in Figure 1.4. The two Lambert transfer arcs, properly defined in Table 1.2. The results are close to the $\Delta V_{\text{Hohmann, total}}$ calculated in section 1.2.

Transfer arc	a [km]	e [\cdot]	i [deg]	Ω [deg]	ω [deg]	θ_{entry} [deg]	θ_{exit} [deg]
Leg 1 (Υ - σ)	1.9483e+08	0.6905	7.6810	19.5680	318.9764	335.5577	212.2848
Leg 2 (σ - A40)	2.1140e+08	0.6673	4.4818	25.9247	306.2919	218.6460	179.9387

Table 1.2: Orbital elements of the two transfer arcs

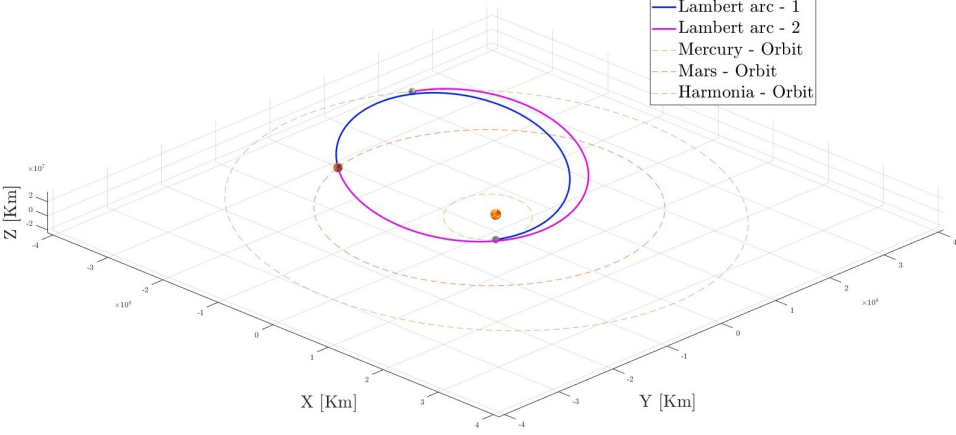


Figure 1.4: Optimal overall mission trajectory

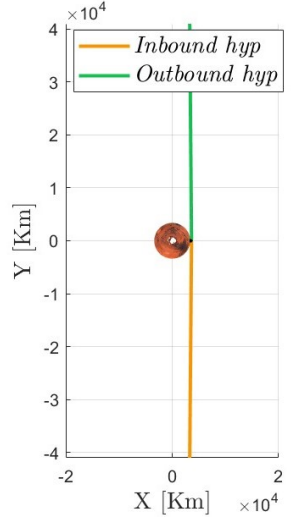


Figure 1.5: Mars flyby

1.6.1. Mars Fly-by

The mission takes advantage of Mars flyby to minimize fuel consumption and efficiently reach its destination. As described in section 1.2, this maneuver requires an impulsive burn ΔV_{PGA} at the common perigee of two intersecting hyperbolic trajectories⁵. The results of this maneuver are summarized in Table 1.3, with the orbital trajectory illustrated in Figure 1.5.

r_{P_σ} [km]	$h_{\text{atm},\sigma}$ [km]	e^- [-]	e^+ [-]	v_∞^- [km/s]	v_∞^+ [km/s]	Δt_{SOI} [s]	ΔV_{PGA} [km/s]	$\ \vec{v}^+ - \vec{v}^-\ $ [km/s]
3613.8976	220.0091	18.0737	18.0737	14.2323	14.2323	8.0979e+04	6.3313e-08	1.5749

Table 1.3: Key parameters for the trajectory calculations.

Furthermore, the eccentricities of the two hyperbola legs are much higher than 1, resulting in $\delta = 6.3435^\circ$. This is because the inbound and outbound velocities have a high magnitude, making Mars' gravitational constant not as influential.

The hyperbola obtained is one that is a trailing flyby, adding energy to the trajectory, thus increasing the semi-major axis. Moreover, the two Lambert arcs have a difference in eccentricities, increasing from the first to the second. The change in inclination can be mainly attributed to the plane of the hyperbola, in comparison to the pericenter impulse. From these results, the optimal combination of two Lambert arcs, we could assess that a single Mars flyby is not so convenient for the purpose of deep space exploration. This because a flyby has as main goal the change of directions without exceeding the mission's budget cost.

The resulting ΔV_{total} of the mission is higher than the propulsive ΔV of any real spacecraft thus far, and making it more feasible would require additional gravity assists, as was the case for numerous missions in history. The overall efficiency of the mission can also be increased by the possibility to include Deep Space Maneuvers (DSMs) [3].

⁵In our result, since the ΔV_{PGA} is very low, nearly all ΔV is saved.

2 | Assignment II: Planetary Explorer Mission

This assignment aims to design a planetary explorer mission around Mercury to perform planetary observation. The carried-out analysis involves the effect of orbit perturbations on the nominal path, the characterization of the ground track, and the proposal of a repeating ground track.

2.1. Orbit Characterization

The nominal trajectory of the spacecraft orbiting around Mercury is defined by the Keplerian parameters shown in Table 2.1 referred to Mercury Equatorial Reference Frame on the 28/3/2041.

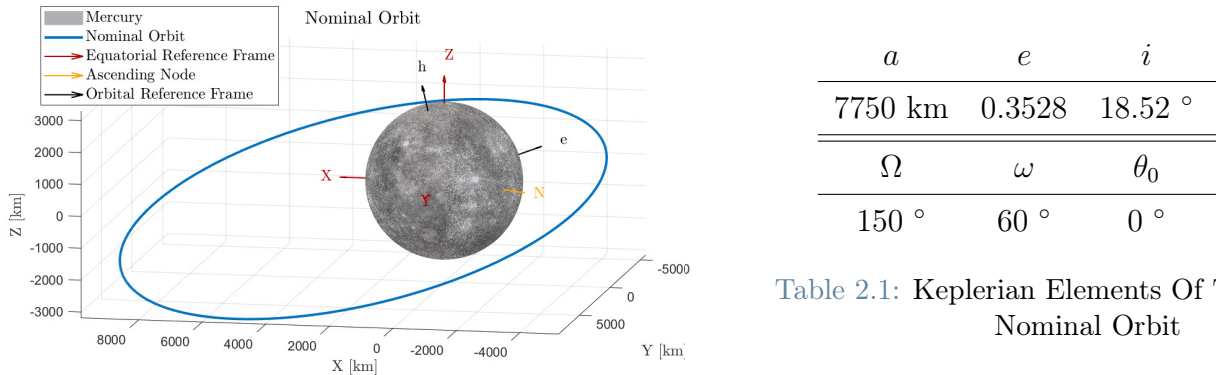


Table 2.1: Keplerian Elements Of The Nominal Orbit

Figure 2.1: Nominal Orbit

The perturbations assumed to be affecting the satellite are:

- *second zonal harmonic J_2 effect*, defined in Cartesian Coordinates as the perturbing acceleration \vec{a}_{J_2} ($J_{2\text{g}} = 5.03 \times 10^{-5}$):

$$\vec{a}_{J_2} = \frac{3}{2} \frac{J_{2\text{g}} \mu_{\text{g}} R_{\text{g}}^2}{r^4} \left[\frac{x}{r} \left(5 \frac{z^2}{r^2} - 1 \right) \hat{i} + \frac{y}{r} \left(5 \frac{z^2}{r^2} - 1 \right) \hat{j} + \frac{z}{r} \left(5 \frac{z^2}{r^2} - 3 \right) \hat{k} \right] \quad (2.1)$$

where: $\vec{r} = x\hat{i} + y\hat{j} + z\hat{k}$ is the spacecraft's position vector with respect to Mercury, [km], μ_{g} is the planetary constant of Mercury, [km^3/s^2], and R_{g} is the mean radius of Mercury, [km].

- *gravitational influence of the Sun* accounted as third-body perturbation:

$$\vec{a}_{\text{Sun}} = \mu_{\odot} \left(\frac{\vec{r}_{\text{SC/Sun}}}{r_{\text{SC/Sun}}^3} - \frac{\vec{r}_{\text{Me/Sun}}}{r_{\text{g/Sun}}^3} \right) \quad (2.2)$$

where: μ_{\odot} is the Sun gravitational constant, [km^3/s^2], $\vec{r}_{\text{SC/Sun}}$ is the position vector of the Sun with respect to the spacecraft and $r_{\text{SC/Sun}}$ is its magnitude, [km], $\vec{r}_{\text{g/Sun}}$ is the position vector of the Sun with respect to Mercury and $r_{\text{g/Sun}}$ is its magnitude, [km].

2.2. Ground Track

The ground track represents the projection of a satellite's trajectory onto the surface of its primary planet, in this case, Mercury. Due to the planet's rotation, the ground track path advances westward by an angle $\Delta\lambda$ depending on spacecraft's orbital period $T_{\text{orb}} = 28880$ s and planetary rotation velocity around its axis ω_\oplus , equal to 1.2399×10^{-6} rad/s = 7.104×10^{-5} deg/s. Since Mercury's rotation is very slow, the shift expected is small considering this orbital period.

(2.3)

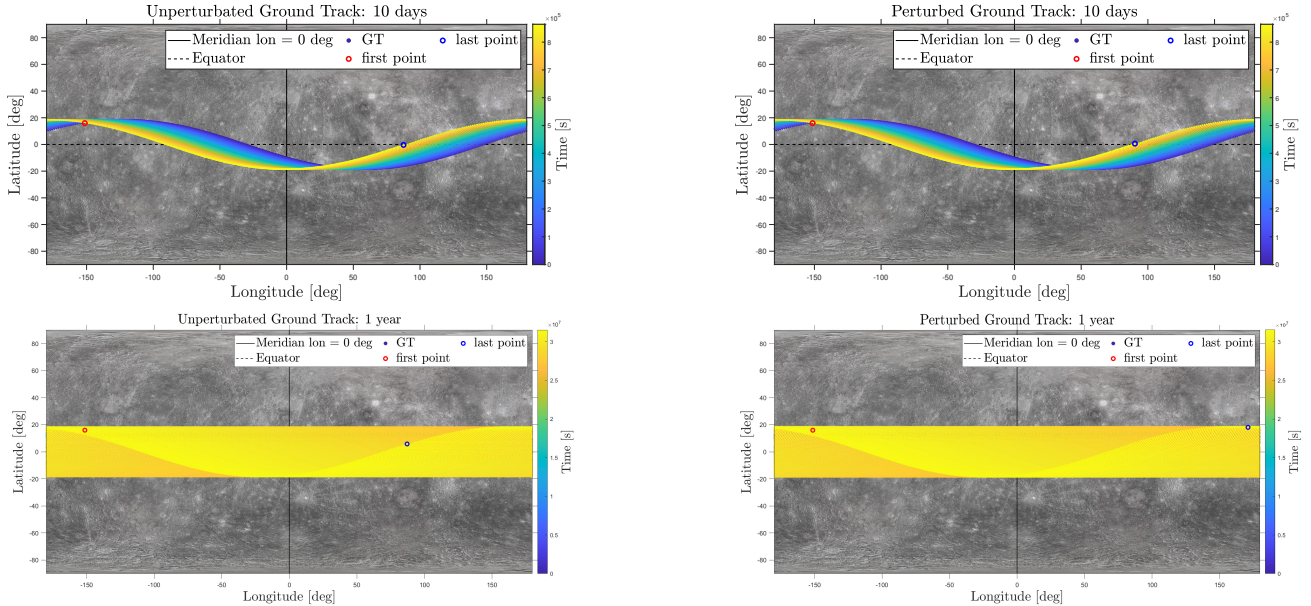


Figure 2.2: Unperturbed and Perturbed Ground Track

As shown in Figure 2.2 over a short period of 10 days, the ground tracks of the unperturbed and perturbed orbits appear nearly identical, with minimal divergence at the final points. However, over a longer period, 1 year, the cumulative effect of perturbations becomes evident, leading to noticeable differences in the final points of the ground tracks but the path during different periods, due to the little value of $\Delta\lambda$, are indistinguishable. A more detailed analysis of the perturbations is done in Section 2.4.

2.3. Repeating Ground Track

To guarantee a repetition over time of the satellite's orbit after k orbits and m rotations of Mercury, the drift of the ground track needs to be equal to the m planet's rotations:

$$k\Delta\lambda = m2\pi \quad (2.4)$$

Exploiting Equation 2.3, it is easy to extrapolate the appropriate orbital period and semi-major axis to obtain a repeating ground track. Imposing $k = 5$ and $m = 3$:

$$T_{\text{orb, rep}} = \frac{2\pi m}{\omega_\oplus k} = 3040416 \text{ s} \quad (2.5)$$

$$a_{\text{rep}} = \left[\mu_\oplus \left(\frac{m}{k\omega_\oplus} \right)^2 \right]^{\frac{1}{3}} = 172790.791 \text{ km} \quad (2.6)$$

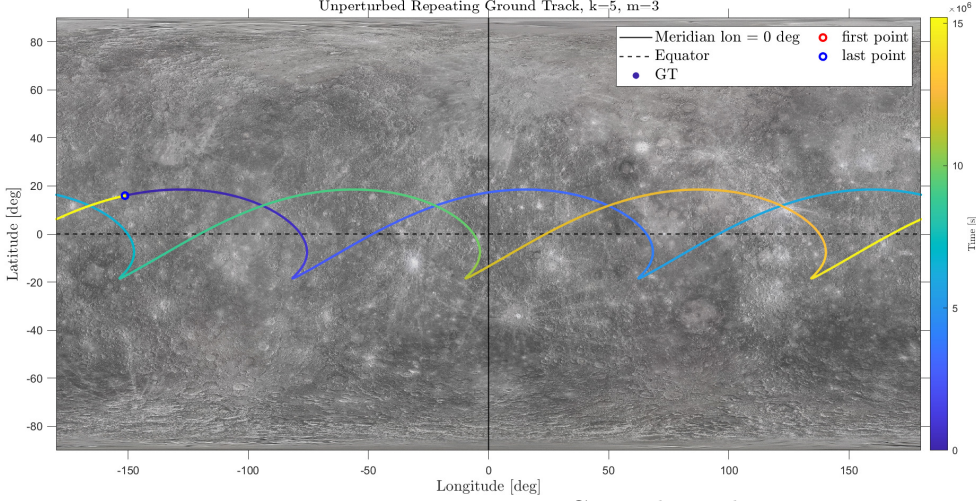


Figure 2.3: Repeating Ground Track

It is fundamental to underline that the apocenter radius r_A is larger than the radius of the Sphere of Influence (SOI) of Mercury $r_{SOI,\text{M}}$ and the pericenter radius r_P is equal to 99.48% of $r_{SOI,\text{M}}$, meaning that the orbit is almost entirely outside the SOI:

$$r_A = 233751.4 \text{ km} \quad r_P = 111830.2 \text{ km} \quad r_{SOI,\text{M}} = r_{\text{M,mean}} \left(\frac{\mu_{\text{M}}}{\mu_{\text{O}}} \right)^{1/2} = 112411.6 \text{ km}$$

Table 2.2: Apocenter, Pericenter and SOI Radius

It is possible to find another k/m ratio that can guarantee to have the orbit apocenter inside the SOI, in order to also guarantee that the hypotheses of application of the Sun perturbation are valid: given Mercury's proximity to the Sun, if the orbit lies outside the Sphere of Influence (SOI), the Sun's perturbation leads to dynamics that deviate from the simpler approximation of a perturbing acceleration. Such behavior indicates that the simplified model is insufficient to accurately describe the motion of the satellite, and suggest the possible implementation of a Three Body problem.

A new valid ratio can be found by applying Equation 2.6 and imposing:

$$r_A = a_{\text{rep}} (1 + e) \leq \eta_{\text{perc}} r_{SOI,\text{M}} \quad \eta_{\text{perc}} = 0.5 \quad (2.7)$$

Spanning values of k and m between 1 and 30 and the possible combinations of k/m , an adequate set of values with the lowest value of k that satisfy the constrain on r_A is: $k = 15$, $m = 1$, $r_A = 54025.72$ km, $a_{\text{rep}} = 39935.481$ km and $T_{\text{orb,rep}} = 337824$ s. As illustrated in Figure 2.4, under the effect of perturbation, the new repeating ground track is not repeating anymore due to the strong effect of the Sun's gravitational influence at this altitude and effect induced on Ω .

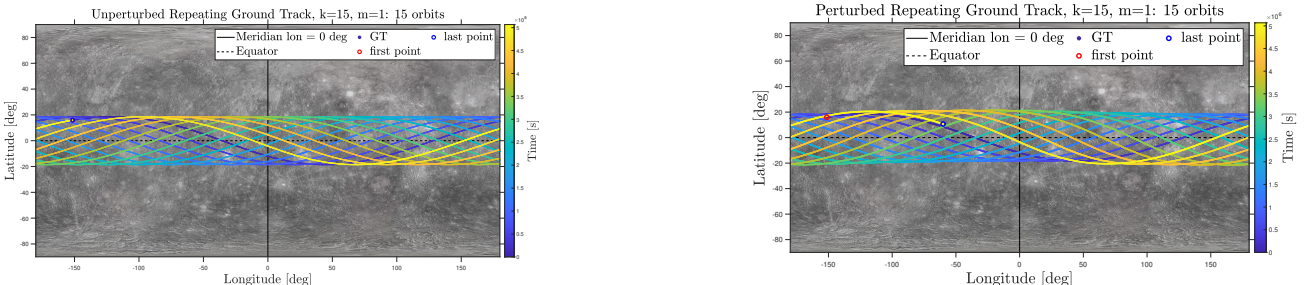


Figure 2.4: Unperturbed and Perturbed Repeating Ground Track

2.4. Perturbed Orbit Propagation

To propagate the orbit defined in Figure 2.1 accounting the perturbations described in Equation 2.1 and Equation 2.2, two different approaches can be applied and compared:

- **Cartesian Equation of Motion integration:** the two-body problem equation of motion is modified by adding the perturbing accelerations in Cartesian Coordinates

$$\ddot{\vec{r}} = -\frac{\mu_{\oplus}}{r^3} \vec{r} + \vec{a}_{J2} + \vec{a}_{Sun} \quad (2.8)$$

- **Gauss Planetary Equations integration:** a numerical method based on a system of six first order ODEs that describes the time evolution of the Keplerian elements over time (\dot{a} , \dot{e} , \dot{i} , $\dot{\Omega}$, $\dot{\omega}$, $\dot{\theta}$) under the effect of the sum \vec{a}_p of the perturbing accelerations expressed in the Radial - Transversal - Out-of-plane reference system (RSW): $\vec{a}_p^{RSW} = a_r \hat{r} + a_s \hat{s} + a_w \hat{w}$

A comparison between those can be made in terms of error in Keplerian parameters' evolution and computational time. Propagating the initial conditions for 1000 orbits (around 334 terrestrial days), a $\Delta t_{step} = T_{orb}/500$, and using a `ode113` solver with the following settings: *Relative Tolerance* = 10^{-13} , *Absolute Tolerance* = 10^{-14} , the maximum errors shown in Table 2.3 are obtained: the error is negligible for all six parameters and has a growing trend with time. In terms of computational time, the Gauss integrator is more efficient than the Cartesian method, with average computational times of: $\Delta t_G = 24.4866$ s and $\Delta t_C = 34.1701$ s as average. The necessity to choose such a large time span is justified by the magnitude of perturbations: J_2 is of the order of 10^{-5} while the Sun perturbation is stronger at higher altitudes. Moreover, Mercury completes its orbit (~ 88) around the Sun multiple times during this time span.

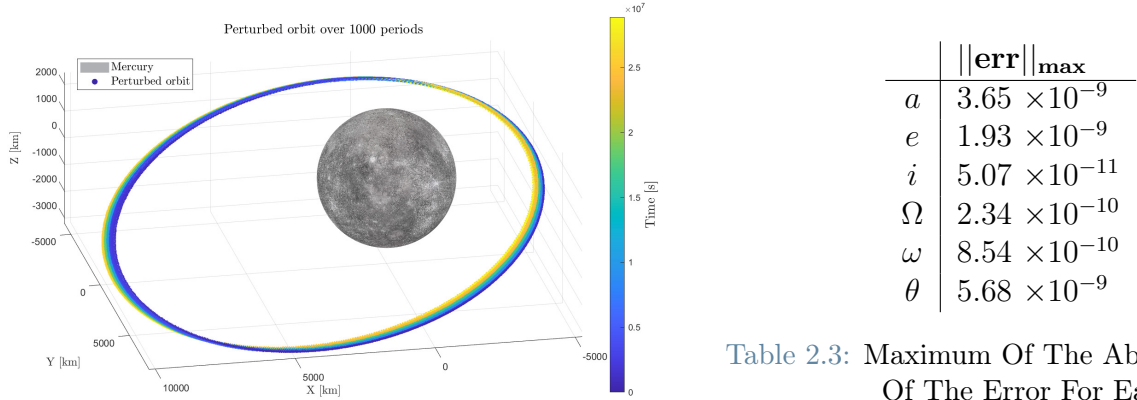


Table 2.3: Maximum Of The Absolute Value Of The Error For Each Orbital Parameter

Figure 2.5: Perturbed Orbit Over 1000 Periods

2.4.1. Results Filtering

The effects of the perturbation on the Keplerian parameters over time are secular, long-period, and short-period variations. Low-pass filters can remove the higher frequency oscillation to highlight the secular and long-period variations. The J_2 perturbation, indeed, acts mainly on the RAAN, the pericenter anomaly, and the mean anomaly introducing a strong secular effect and the principal results of the third-body perturbation are secular and long periodic variations of inclination, eccentricity, RAAN, and pericenter anomaly. Neither one of the two perturbations taken into account is expected to have a secular effect on the semi-major axis. In fact, only short-period

oscillations are detected. To avoid discontinuities in the true anomaly analysis, the values have been unwrapped so that the values continuously grow with time while affected by short-period variations. In the other graphics, it is possible to see both short and long-periodical variations and the predominant increasing or decreasing behavior of the parameters thanks to different cut-off frequencies for the filtering process.

	a	e	i	Ω	ω	θ
f [Hz]	1.73×10^{-6}	1.73×10^{-4}				
f [Hz]	-	7.7×10^{-6}	7.7×10^{-6}	7.7×10^{-6}	7.7×10^{-6}	-

Table 2.4: Cut-off Frequencies For Filter 1 and Filter 2

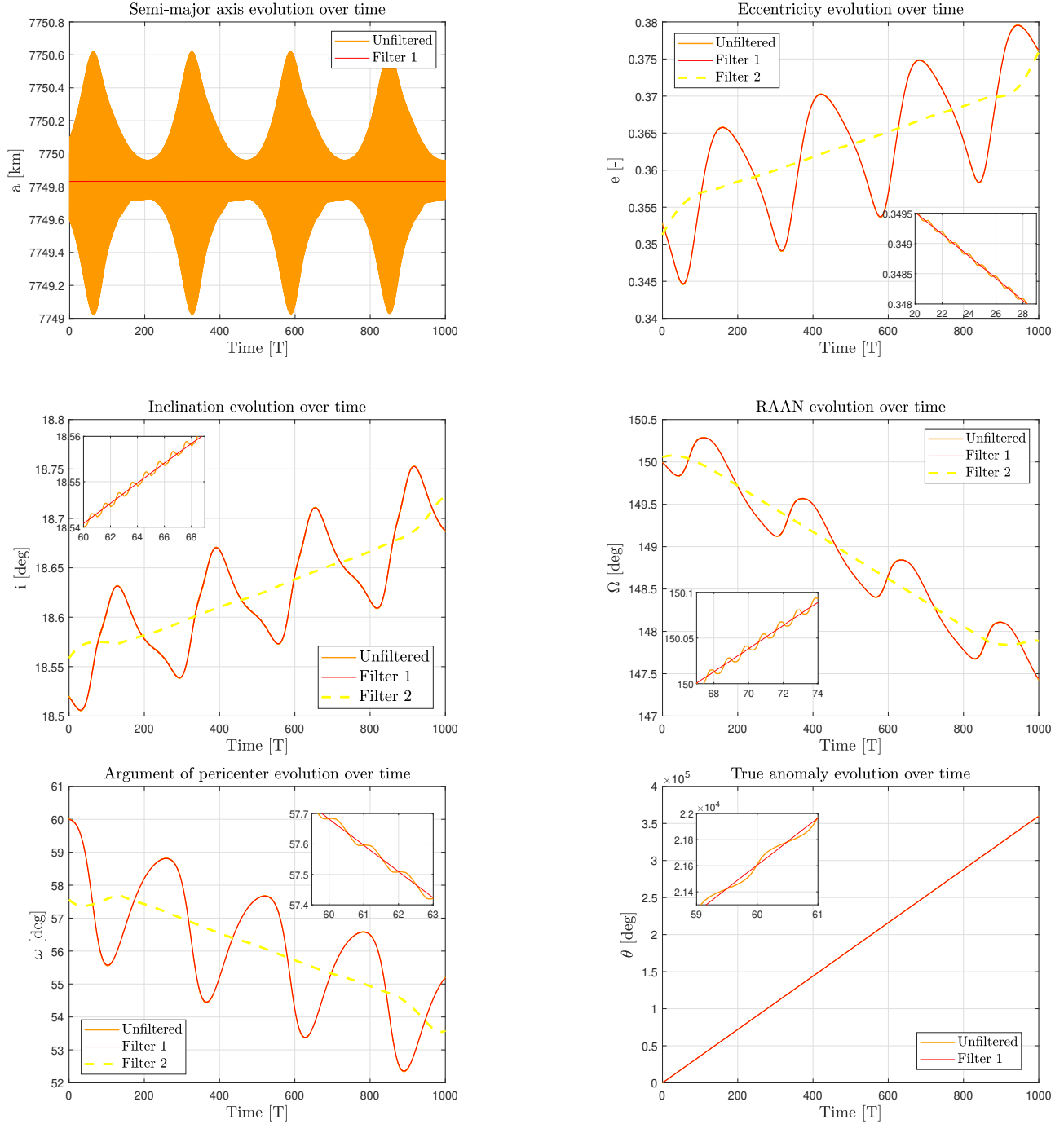


Figure 2.6: Keplerian parameter evolution over time and filtering

As the Sun perturbation is known to have secular effects over longer periods of time, the predominant trend may change and reveal a different trend (a variation in ω has been found in 20000 T_{orb} , but to detect this effect more clearly the propagation should be conducted for more than 20000 orbits, but due to limited performances of the hardware available this was not possible).

2.5. Real World Data Analysis

A real data analysis is necessary to understand if the theoretical predictions align with real-case scenarios. To complete this analysis two objects orbiting around the Earth have been chosen. Their TLEs have been downloaded from Space-Track [4] to retrieve the ephemerides from NASA Horizons System [5]. The data correspond to the time span of 365 days from 2024/1/1 0:00:00 h.

- Alouette-2, a Canadian satellite for ionosphere, launched on November 29th, 1965 and dismissed August 1st, 1975. The satellite orbits in a region among LEO and MEO ($r_p = 6885.3$ km, $r_a = 8977.5$ km) [6]
- IMAGE (Imager for Magnetopause-to-Aurora Global Exploration) a NASA satellite for the study of magnetosphere and ionosphere, launched on March 25th, 2000 and now inactive. The satellite orbits on a High Elliptical Orbit ($r_p = 7785$ km, $r_a = 51813.8$ km) [6]

Alouette-2 (Figure 2.7) Considering the altitude, the perturbations are due to the J_2 effect and aerodynamic drag below 800 km, while above solar radiation pressure (SRP) gets stronger [7]. The J_2 effect, discussed in detail in subsection 2.4.1, remains the most significant. Drag, together with SRP, causes secular variations in a , e , i . Aerodynamic drag also induces long-periodic variations in i , Ω , ω , while SRP leads to periodic variations in a and e and secular on Ω and ω . Specifically, SRP causes a and e to decrease when the satellite moves towards the Sun and increase when it moves away [7]. The semi-major axis, apart from a strong short-period has a light decreasing trend as expected for drag influence while eccentricity is only oscillating. Since $63.4^\circ < i < 90^\circ$, the results show the regression of the node ($\dot{\Omega} < 0$) and perigee regression ($\dot{\omega} < 0$) under the influence of J_2 as expected [7]. Inclination shows a short-period variation and a long-period oscillation that can be justified by drag effects in the lowest region of the orbit.

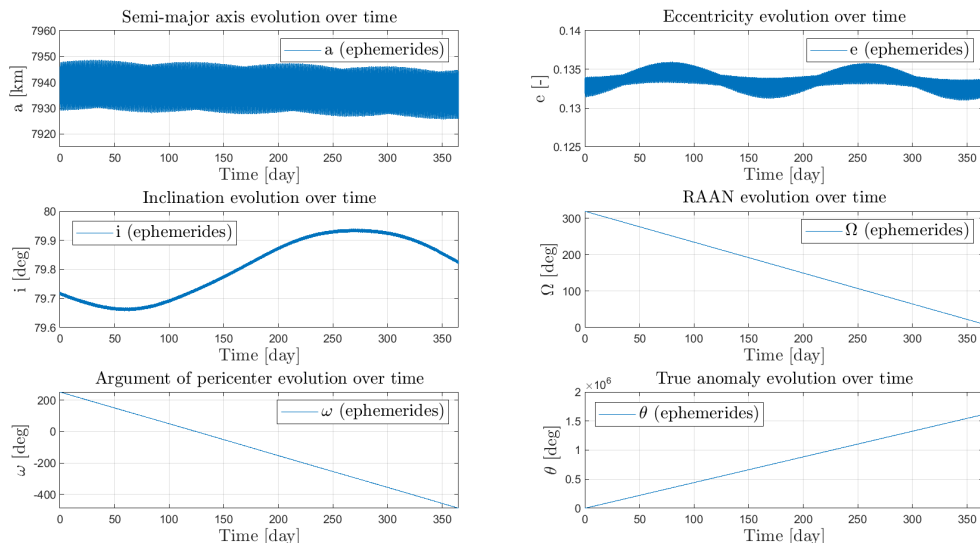


Figure 2.7: Alouette-2 Keplerian Parameters Evolution

IMAGE (Figure 2.8) In HEO, the influence of third-body perturbation (Sun and Moon) is significant and coupled with the aerodynamic drag, that affects the spacecraft in the perigee region, intensifies the effects of the latter [7]. The increase in e can be justified by the eccentricity growth of the orbit induced by SRP that acts strongly in the further regions from Earth. Given $90^\circ < i < 116.6^\circ$, ω and Ω behave exactly as expected if J_2 would be the predominant influence ($\dot{\Omega} > 0$, $\dot{\omega} < 0$) [7], an assumption that theoretically is not true for HEO orbit. The effect of the third-bodies is seen in the inclination (long-period oscillation, also influenced by drag) but is not seen in Ω and ω .

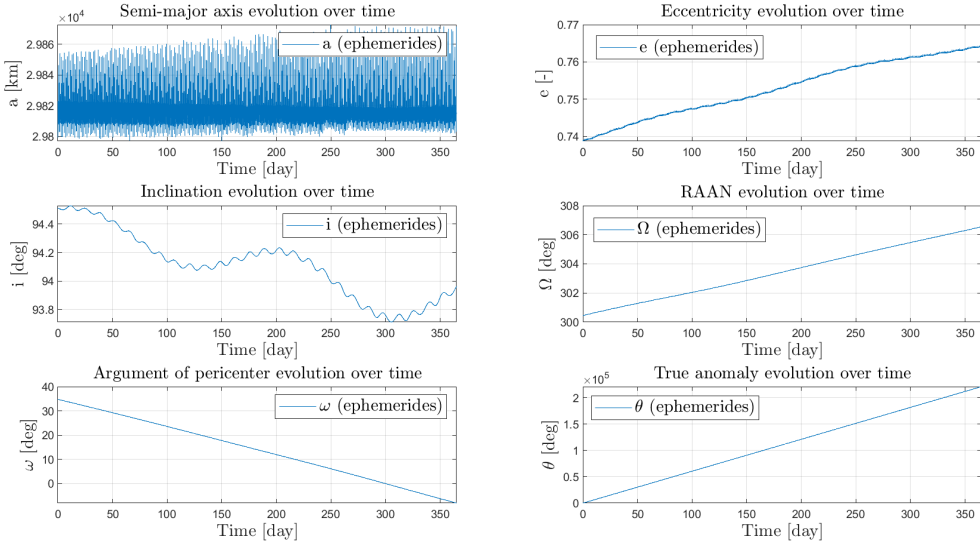


Figure 2.8: IMAGE Keplerian Parameters Evolution

The theoretical expectations and hypotheses proved to be reasonably accurate, particularly for the Alouette-2 satellite, while some adjustments are necessary for the IMAGE satellite. These discrepancies can be attributed to approximations in the mathematical models, challenges in estimating parameters such as atmospheric density and relative velocity for drag, the exclusion of the Moon's influence as a three-body problem, and inaccuracies in determining the relative positions of the spacecraft and attractors. Additionally, a more in-depth analysis of the coupling effects between different perturbations is needed to account for variations in theoretical predictions, both when perturbations act individually and when one is more dominant than the other based on attitude (e.g., in a HEO orbit). Therefore, while theoretical predictions provide a useful general approach, they are insufficient to fully capture most real-world scenarios.

References

- [1] Laura M. Burke, Robert D. Falck, and Melissa L. McGuire. *Interplanetary mission design handbook: Earth-to-mars mission opportunities 2026 to 2045*. NASA, 2010.
- [2] Howard D Curtis. *Orbital mechanics for engineering students*. Butterworth-Heinemann, 2019. ISBN: 9780081021330.
- [3] Robin Biesbroek. “Deep-Space Maneuvers”. In: *Lunar and Interplanetary Trajectories*. Springer International Publishing, 2016. ISBN: 978-3-319-26983-2.
- [4] STR. *SPACE TRACK*. URL: <https://www.space-track.org/auth/login>.
- [5] NASA Jet Propulsion Laboratory. *Horizon*. URL: <https://ssd.jpl.nasa.gov/horizons/>.
- [6] WMO. *OSCAR*. URL: <https://space.oscar.wmo.int/satellites>.
- [7] David A. Vallado. *Fundamentals of Astrodynamics and Applications*. McGraw-Hill, 1997.